Fabrication and optical characterization of gold-infiltrated silica opals

2005 J. Phys.: Condens. Matter 17 2177

(http://iopscience.iop.org/0953-8984/17/13/015)

INSTITUTE OF PHYSICS PUBLISHING JOURNAL OF PHYSICS: CONDENSED MATTER

J. Phys.: Condens. Matter **17** (2005) 2177–2190 doi:10.1088/0953-8984/17/13/015

Fabrication and optical characterization of gold-infiltrated silica opals

Wenjiang Li, Gang Sun, Fangqiong Tang, Wing Yim Tam, Jensen Li, C T Chan and Ping Sheng

Department of Physics, Hong Kong University of Science and Technology, Clear Water Bay, Kowloon, Hong Kong, People's Republic of China

Received 8 September 2004, in final form 23 February 2005
Published 18 March 2005
Online at stacks.iop.org/JPhysCM/17/2177

Abstract

We report the fabrication of metal-infiltrated silica opals for optical studies. Highly mono-dispersed silica microspheres are fabricated and assembled by a force packing method to form opals with large domain sizes. The opals are then infiltrated with gold by an electroplating technique. The optical properties of the infiltrated opals in the visible range are studied and model calculations based on a multiple-scattering formalism are used to interpret the experimental results. The calculated position of the directional gap of the silica opal agrees very well with experimental observation. We found that the optical properties of the infiltrated sample can be explained using a model system in which the voids in the silica opal are partially filled with Au and the surface of the slab is covered with a thin layer of Au.

1. Introduction

Photonic band gap materials have attracted considerable interest from both the science and engineering communities, due to their potential applications. Photonic band gap materials generally do not exist in nature and have to be fabricated artificially. These materials possess the unique property of having band gaps in which electromagnetic waves cannot propagate, analogous to the forbidden gaps in semiconductors [1]. Photonic band gap materials are usually realized in two-component dielectric media with a periodic variation in the refractive index. A few promising routes followed for making photonic band gap (PBG) crystals in the IR/optical frequency regimes include microfabrication [2], inverse-opal and related techniques [3], and laser lithography [4]. These methods, while different in practice, all seek to create pre-defined artificial periodic arrays of high dielectric constant materials, with the resulting Bragg scattering serving to manipulate the flow of light. While most of these artificial materials are based on dielectrics, metallo-dielectric materials constitute an interesting alternative [5, 6]. By using the metallo-dielectric systems, band gaps have been realized in the microwave regime, with good agreements obtained between theory and experiment [6].

Among the various methods used to create a periodic structure, the self-assembly of artificial opal from microspheres is perhaps the easiest and the most economical. However, this method has its limitations. The self-assembled structure is always close-packed FCC. The structural variation degree of freedom is thus rather limited. In addition, the quality of the periodic structure depends very much on the availability of mono-dispersed spheres, which again limits the choice of materials to silica or polymeric materials. However, artificial opal can be viewed as a microporous (or nanoporous) medium ideal for infiltration with another material via a variety of methods, thereby modifying its optical properties. It is the purpose of this article to explore the optical properties of silica opals infiltrated with gold through an electroplating technique [7]. While an idealized structure is that of glass spheres embedded in a solid gold host, we found that for a reasonably thick (say 20 layers) opal, infiltration resulted in a fairly low concentration of gold inside the voids, so that the resulting composite is better described as a metal–dielectric–vacuum three-phase composite. Through simulations we were able to correlate the optical properties of such a system with a reasonable structural model. Our work is an example in which experiment and simulation can go hand in hand to improve an understanding of the optical properties of a composite system from a structural model. In what follows, details of the fabrication of and optical measurements on the infiltrated opals are presented in section 2, followed by theoretical modelling and comparison with the experimental results in section 3. A summary is presented in section 4.

2. Experiment

Monodispersed silica spheres were prepared by the Stöber method [8]. Silica particle seeds of 27 nm (Ludox from Aldrich) were first dispersed in an ethanol (99.7%)–ammonia (25–28%) solution. Then tetraethyl orthosilicate (TEOS, 98% reagent grade) was slowly added into the seed solution at 30 °C under mild stirring. The final solution contained 7.3 mol l^{-1} ethanol, 1.95 mol l^{-1} ammonia, and 0.9 mol l^{-1} TEOS. Tetraethyl orthosilicate was hydrolysed to form larger silica particles from the seeds and, following ageing in the solution for 5 h under stirring, mono-dispersed silica spheres were obtained. The microspheres had dispersion of less than 5% as determined by transmission electron micrography.

To fabricate the opal needed for infiltration, we used a force packing method that was successfully employed in fabricating large scale multilayered opals [9, 10]. The details of the packing method have been reported already for larger particles [10]. Figure 1 shows a schematic diagram for the force packing method. Two glass plates formed the top and bottom plates of the chamber. The bottom glass plate was first sputtered with a layer of 15 nm gold or 50 nm indium–tin oxide (ITO) to serve as an electrode. A square frame (1.5×1.5 cm^2) of 2.8 μm thick photoresist was then deposited onto the plate forming the side walls of the chamber. At one side of the frame, 0.1 μm deep and 200 μm wide trenches were etched out of the photoresist. These trenches allowed fluid to pass, but restrained the packing particles once the top glass plate was installed. The top glass plate had a small hole with a glass tube attached which was connected to a nitrogen gas supply at a controlled pressure through rubber tubing. The glass tube provided the inlet for introducing particles into the chamber. The top and the bottom glass plates were held together by binder clips to form a thin chamber such that the chamber formed was completely sealed except at the side with the trenches. A dilute water suspension of 0.25 μm silica microspheres fabricated as above was introduced into the chamber by injecting through the rubber tubing with a syringe whilst nitrogen flowed slowly through the chamber. Since the particles were small enough, Brownian motion was enough to prevent sedimentation and thus sonication was not needed, in contrast to the case for packing of larger and heavier particles [10]. The silica spheres began to assemble themselves starting

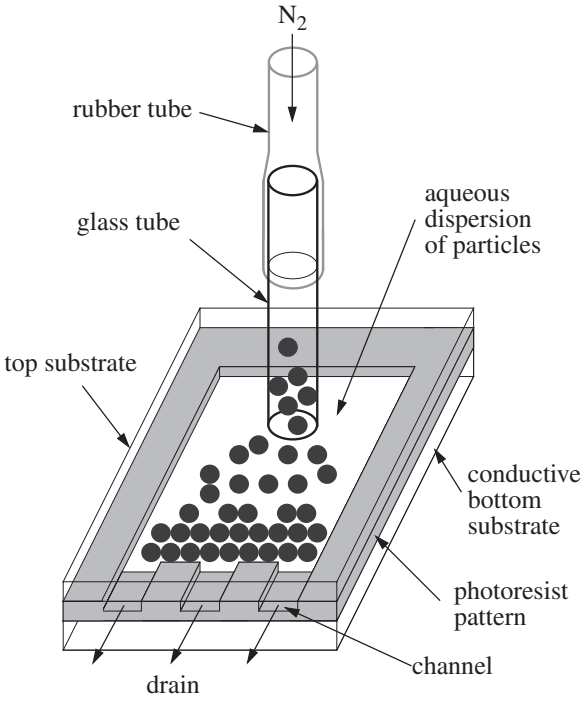

Figure 1. Schematic diagram of the force packing set-up.

at the side with the trenches. Several injections might be needed to obtain a large working area of ordered structure. After the sample had reached a workable size, the filling process was stopped and the whole assembly was allowed to dry in open air. Domains of single crystals with size of about $50 \times 50\ \mu m^2$ were easily obtained. The sample was checked for optical properties before the infiltration process was carried out.

The infiltration was carried out by an electroplating technique. An electroplating solution of 2 mg ml^{-1} potassium gold cyanide was first introduced into the chamber through the glass tube. A platinum strip, placed inside the glass tube, was used as the anode while the gold or ITO layer plated on the bottom glass plate served as the cathode. The infiltration was carried out using a constant current of 20 μA and the plating solution was replenished a few times to obtain thicker coatings. After the deposition, the sample was washed with distilled water and dried in open air. The infiltrated opal showed regions of reddish to yellowish-gold reflections indicating different levels of infiltration over the sample. Figure 2 shows SEM images of the infiltrated opal before (figure 2(a)) and after (figures 2(b) and (c)) five short depositions such that for each deposition the sample was washed, dried, and measured optically before the subsequent deposition using fresh plating solution. On comparing figures 2(a) and (b) and (c), it is clear that Au was deposited onto the substrate (figure 2(c)) and the silica spheres (figure 2(b)) even though the Au coating was not smooth. The TEM image (figure 2(d)) shows that the infiltrated Au has a porous structure in the voids of the opal. In addition, diffraction showed that the Au was polycrystalline. Figures 3(a) and (b) show SEM images of infiltrated opal after a single 3 h long deposition until all the Au content in the plating solution was used up. They show regions of different Au infiltrations. It was found that further plating by adding new solution did not increase the Au content inside the opal much but it increased the Au layer on the top of the opal as shown in figure 3(c). This could be explained by the fact that once the Au in the solution filling the interstitial spaces between the microspheres was used up to

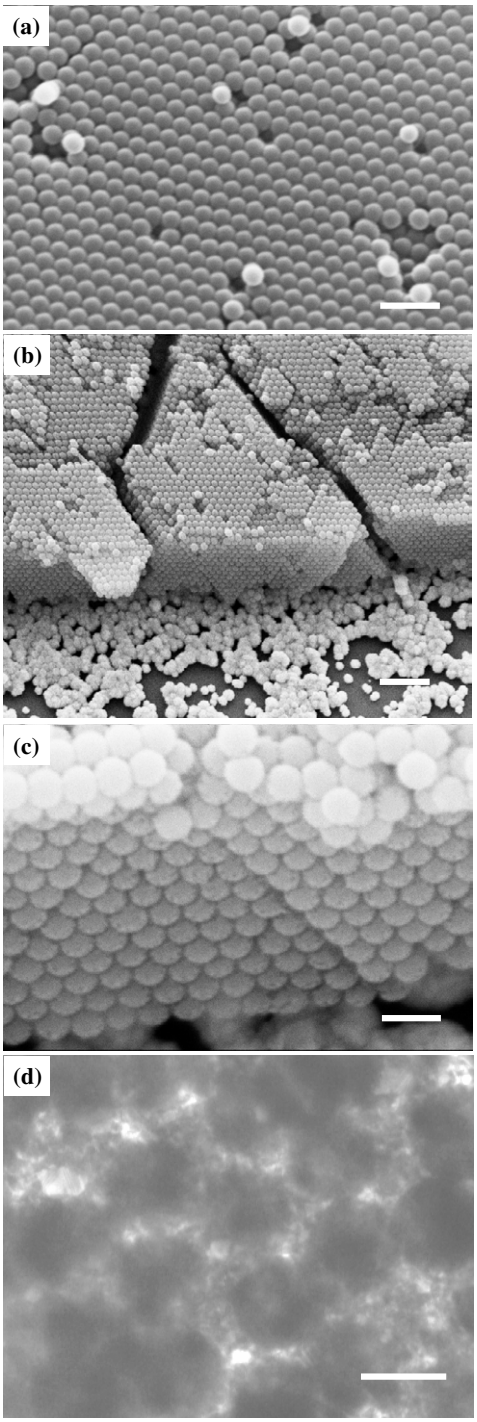

Figure 2. SEM images of silica opal (a) before and ((b), (c)) after five short depositions, corresponding to a total of 600 s plating time, of Au infiltration by electroplating; (d) is a TEM image of the infiltrated silica opal after a single 3 h deposition. The scale bars are (a) 0.6, (b) 2.0, (c) 0.4, and (d) 0.2 μm.

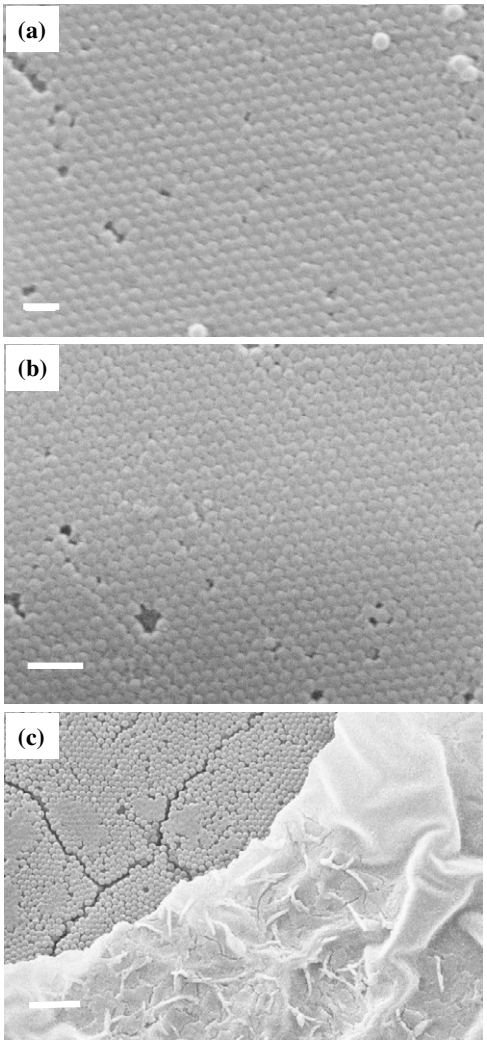

Figure 3. SEM images of an Au-infiltrated silica opal slab—((a), (b)) after a single 3 h electroplating without replenishing the plating solution; (c) re-plated by replenishing the plating solution after the 3 h plating as in (a) and (b). The scale bars are (a) 0.6, (b) 1.0 and (c) 2.0 μm.

form a porous structure, it was difficult to get new Au solution to replenish the inner spaces of the porous structure to increase the Au content. However, more concentrated plating solutions could be used to get higher Au filling ratios.

The reflectance and transmittance of the infiltrated opals were measured at normal incidence using an optical microscope (Olympus BX60) coupled to a spectrometer (Oriel Cornerstone TM260) through an optical fibre. The microscope, with a pinhole installed in the optical path, can sample an area down to 50×50 μm^2 (about the size of a single domain of the packed microspheres) using a $20\times$ objective. Because of the reduced intensity after passing through the pinhole a frequency locking technique was used to increase the sensitivity of the optical measurements. In order not to disturb the opal before subsequent infiltration the measurements were performed without removing the top glass plate. Before each optical measurement, the sample was washed a few times with distilled water to remove

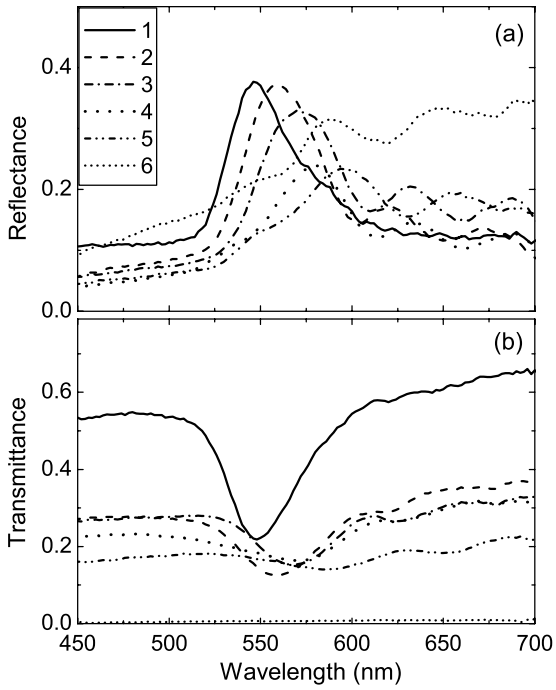

Figure 4. Measured reflectance (a) and transmittance (b) of infiltrated silica opal at difference times, without removing the top glass plate. The curves are for: (1) bare silica opal, and after (2) 10 s, (3) 20 s, (4) 60 s, (5) 300 s, (6) 600 s.

the residue of plating solution left from previous infiltration. Reflectance and transmittance were normalized against backgrounds of silver mirror reflection and empty air transmission, respectively. Figure 4 shows the normalized reflectance and transmittance of a multiply Au-infiltrated opal in the (111) direction[1]. The different curves shown are results obtained at the same region of the opal for different plating times as stated in the previous paragraph with the longest time corresponding to figures 2(b), (c). The observed partial gap shifts progressively to longer wavelengths with the plating time, corresponding to increase of the Au content. However, at the latest time, the red shift stops, and this is accompanied by an increase of reflectance. In addition to the main reflectance peak (as observed in the reflectance), multiple peaks or oscillations are also observed for the infiltrated opal. Figure 5 shows results taken from two different areas (corresponding to images of figures 3(b) and (c)) of the same sample with a single long deposition. The bare opal results (solid curves) and the reflection of a gold mirror (long dashed curve) are included for comparison. We note that the bare opal and the infiltrated opal are two different samples. The infiltrated opal results are similar to those for the latest time in figure 4.

3. Model

While the measured spectra shown in figures 4 and 5 are rather complex at first sight, they can nevertheless be understood qualitatively with the help of numerical modelling. To this end, we consider a prototypical system as shown schematically in figure 6. We employ the multiple-

[1] The [111] orientation of the opal was identified from SEM images taken after the last infiltration.

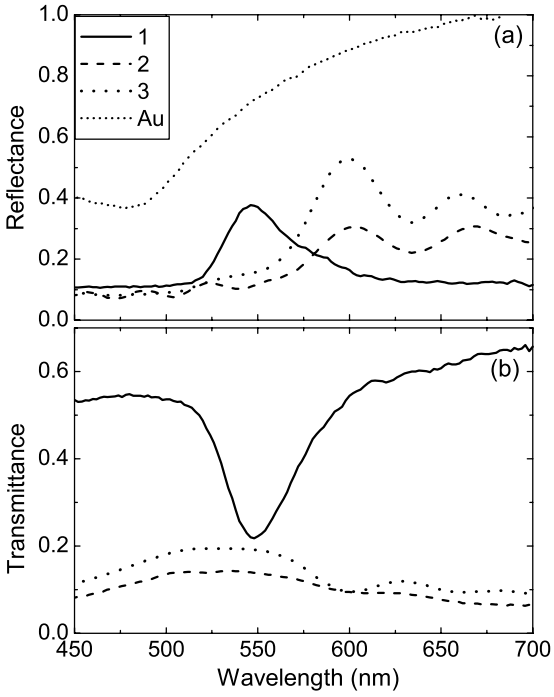

Figure 5. Measured reflectance (a) and transmittance (b) of infiltrated silica opal at two areas of a sample after a single long plating, compared with those for the bare silica opal. (1) The solid curve is for bare silica opal (from figure 4); (2) and (3) are for figures 3(a) and (b), respectively. The Au line corresponds to reflection of an Au mirror. We note that the bare silica opal and the infiltrated silica are two different samples. Also the measurements for the infiltrated opals were carried out with the top glass plate removed.

scattering techniques of Stefanou *et al* to calculate the reflectance and transmittance [11, 12]. In the multiple-scattering method, the incident and the scattered electric and magnetic fields by spherical objects are expanded in vector spherical harmonics. For a plane incident wave scattered by a single sphere with radius S, the total wavefield outside the sphere is

$$\mathbf{E}(\mathbf{r}) = \sum_{l=1}^{\infty}\sum_{m=-1}^{l}\left\{\frac{\mathrm{i}}{q}a_{lm}^{0\mathrm{E}}\nabla\times j_l(qr)\mathbf{X}_{lm}(\hat{\mathbf{r}}) + a_{lm}^{0\mathrm{H}}j_l(qr)\mathbf{X}_{lm}(\hat{\mathbf{r}}) + \frac{\mathrm{i}}{q}T_l^{\mathrm{E}}a_{lm}^{0\mathrm{E}}\nabla\times h_l^{+}(qr)\mathbf{X}_{lm}(\hat{\mathbf{r}}) + T_l^{\mathrm{H}}a_{lm}^{0\mathrm{H}}h_l^{+}(qr)\mathbf{X}_{lm}(\hat{\mathbf{r}})\right\}, \tag{1}$$

$$\mathbf{H}(\mathbf{r}) = \sqrt{\frac{\varepsilon}{\mu}}\sum_{l=1}^{\infty}\sum_{m=-1}^{l}\left\{a_{lm}^{0\mathrm{E}}j_l(qr)\mathbf{X}_{lm}(\hat{\mathbf{r}}) - \frac{\mathrm{i}}{q}a_{lm}^{0\mathrm{H}}\nabla\times j_l(qr)\mathbf{X}_{lm}(\hat{\mathbf{r}}) + T_l^{\mathrm{E}}a_{lm}^{0\mathrm{E}}h_l^{+}(qr)\mathbf{X}_{lm}(\hat{\mathbf{r}}) - \frac{\mathrm{i}}{q}T_l^{\mathrm{H}}a_{lm}^{0\mathrm{H}}\nabla\times h_l^{+}(qr)\mathbf{X}_{lm}(\hat{\mathbf{r}})\right\}, \tag{2}$$

where ε and μ are the permittivity and magnetic permeability outside the sphere, respectively, and $q = \sqrt{\mu\varepsilon}\,\omega/c$ is the magnitude of the wavevector outside the sphere. In the equations, $j_l(qr)$ and $h_l^{+}(qr)$ are the spherical Bessel and Hankel (outgoing) functions, respectively, and $\mathbf{X}_{lm}(\hat{\mathbf{r}})$ are vector spherical harmonics defined by $\sqrt{l(l+1)}\mathbf{X}_{lm}(\hat{\mathbf{r}}) = \mathbf{L}Y_{lm}(\mathbf{r}) = -\mathrm{i}\mathbf{r}\times\nabla Y_{lm}(\mathbf{r})$.

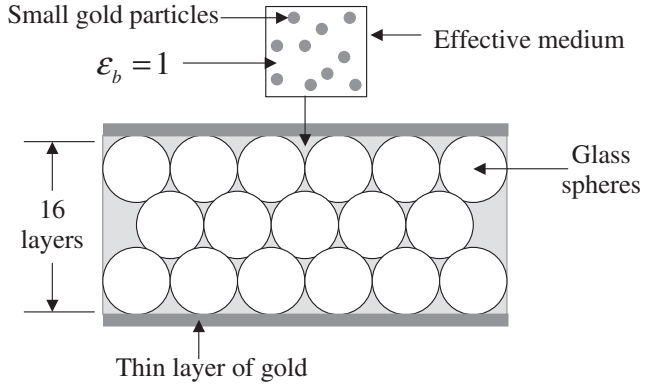

Figure 6. A schematic diagram illustrating the model used to simulate the experiment.

In equations (1) and (2), the first two terms correspond to the field of an incident plane wave, while the last two terms correspond to the scattered wave, in which the coefficients T_l^{E} and T_l^{H} are given by

$$T_l^{\mathrm{E}}(\omega) = \left. \frac{j_l(q_s r)\frac{\partial}{\partial r}(r j_l(qr))\varepsilon_s - j_l(qr)\frac{\partial}{\partial r}(r j_l(q_s r))\varepsilon}{h_l^+(qr)\frac{\partial}{\partial r}(r j_l(q_s r))\varepsilon - j_l(q_s r)\frac{\partial}{\partial r}(r h_l^+(qr))\varepsilon_s} \right|_{r=S}, \tag{3}$$

$$T_l^{\mathrm{H}}(\omega) = \left. \frac{j_l(q_s r)\frac{\partial}{\partial r}(r j_l(qr))\mu_s - j_l(qr)\frac{\partial}{\partial r}(r j_l(q_s r))\mu}{h_l^+(qr)\frac{\partial}{\partial r}(r j_l(q_s r))\mu - j_l(q_s r)\frac{\partial}{\partial r}(r h_l^+(qr))\mu_s} \right|_{r=S}, \tag{4}$$

where ε_s and μ_s are the permittivity and magnetic permeability of the sphere, respectively, and $q_s = \sqrt{\mu_s \varepsilon_s}\omega/c$ is the magnitude of the wavevector in the sphere. If the plane incident wave is scattered by a plane of spheres, the total wavefield can be written in the following form:

$$\begin{aligned}\mathbf{E}(\mathbf{r}) = \sum_{l=1}^{\infty}\sum_{m=-1}^{l}\Bigg\{ & \frac{\mathrm{i}}{q} a_{lm}^{0\mathrm{E}} \nabla \times j_l(qr)\mathbf{X}_{lm}(\hat{\mathbf{r}}) + a_{lm}^{0\mathrm{H}} j_l(qr)\mathbf{X}_{lm}(\hat{\mathbf{r}}) \\ & + \frac{\mathrm{i}}{q} b_{lm}^{+\mathrm{E}} \nabla \times \sum_{\mathbf{R}_n} \exp(\mathrm{i}\mathbf{k}_\parallel \cdot \mathbf{R}_n) h_l^+(qr)\mathbf{X}_{lm}(\hat{\mathbf{r}}) \\ & + b_{lm}^{+\mathrm{H}} \sum_{\mathbf{R}_n} \exp(\mathrm{i}\mathbf{k}_\parallel \cdot \mathbf{R}_n) h_l^+(qr)\mathbf{X}_{lm}(\hat{\mathbf{r}}) \Bigg\},\end{aligned} \tag{5}$$

$$\begin{aligned}\mathbf{H}(\mathbf{r}) = \sqrt{\frac{\varepsilon}{\mu}} \sum_{l=1}^{\infty}\sum_{m=-1}^{l}\Bigg\{ & a_{lm}^{0\mathrm{E}} j_l(qr)\mathbf{X}_{lm}(\hat{\mathbf{r}}) - \frac{\mathrm{i}}{q} a_{lm}^{0\mathrm{H}} \nabla \times j_l(qr)\mathbf{X}_{lm}(\hat{\mathbf{r}}) \\ & + b_{lm}^{+\mathrm{E}} \sum_{\mathbf{R}_n} \exp(\mathrm{i}\mathbf{k}_\parallel \cdot \mathbf{R}_n) h_l^+(qr)\mathbf{X}_{lm}(\hat{\mathbf{r}}) \\ & - \frac{\mathrm{i}}{q} b_{lm}^{+\mathrm{H}} \nabla \times \sum_{\mathbf{R}_n} \exp(\mathrm{i}\mathbf{k}_\parallel \cdot \mathbf{R}_n) h_l^+(qr)\mathbf{X}_{lm}(\hat{\mathbf{r}}) \Bigg\}.\end{aligned} \tag{6}$$

The coefficients $b_{lm}^{+\mathrm{E}}$ and $b_{lm}^{+\mathrm{H}}$ can obtained by solving the following equation:

$$\begin{pmatrix} \mathbf{I} - \mathbf{T}^{\mathrm{E}}\boldsymbol{\Omega}^{\mathrm{EE}} & \mathbf{T}^{\mathrm{E}}\boldsymbol{\Omega}^{\mathrm{EH}} \\ \mathbf{T}^{\mathrm{H}}\boldsymbol{\Omega}^{\mathrm{HE}} & \mathbf{I} - \mathbf{T}^{\mathrm{H}}\boldsymbol{\Omega}^{\mathrm{HH}} \end{pmatrix} \begin{pmatrix} \mathbf{b}^{+\mathrm{E}} \\ \mathbf{b}^{+\mathrm{H}} \end{pmatrix} = \begin{pmatrix} \mathbf{T}^{\mathrm{E}}\mathbf{a}^{0\mathrm{E}} \\ \mathbf{T}^{\mathrm{H}}\mathbf{a}^{0\mathrm{H}} \end{pmatrix}, \tag{7}$$

where $\boldsymbol{\Omega}$ depends on the geometry of the plane. The scattered wave of equations (5) and (6) can be expressed as a sum of plane waves, and the scattering by multiple planes of spheres can be treated by the transfer matrix technique. The multiple-scattering method can handle

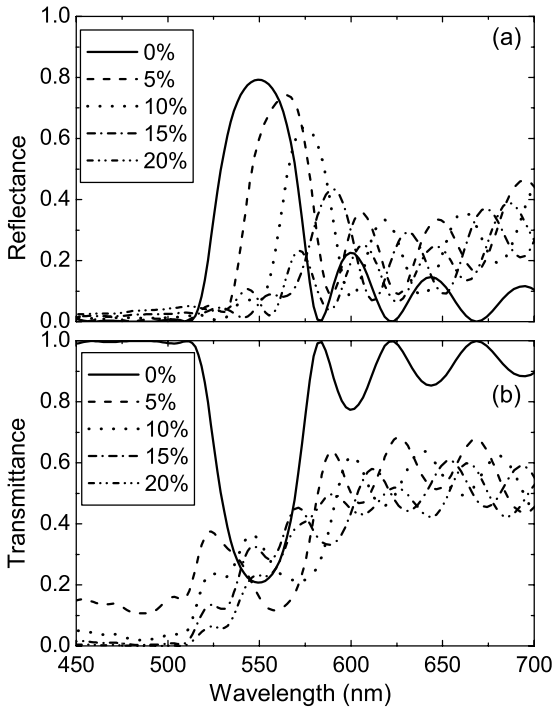

Figure 7. Calculated reflectance and transmittance of a 16-layer Au-infiltrated silica opal for different filling ratios.

very effectively the scattering properties of spherical objects, and can predict the reflectance and transmittance of a slab of finite thickness [13]. We obtain convergence with respect to the angular momentum index in the vector spherical harmonics expansion by increasing $L_{\max}$ until it convergences (up to $L_{\max} = 19$ has been used). The inputs in the calculation are the geometry (how the spheres are arranged) and the dielectric function of the spheres and its embedding medium. The dielectric functions of silica and Au are taken from experimental data [13]. We note that the multiple-scattering formalism automatically incorporates absorption.

We first consider the optical property of a slab of bare silica spheres. The silica spheres with diameters of 0.25 μm are arranged in a close-packed FCC structure with the surface normal along the (111) direction. The calculated results for reflectance and transmittance of a 16-layer slab are shown as the solid curves in figures 7(a) and (b) respectively. We see a strong reflectance peak and a corresponding transmittance dip at about 550 nm, and this is the consequence of a direction gap in the [**111**] direction. The position of the calculated reflectance peak agrees very well with that observed in the experiment (see the solid curve in figure 4). We also see some oscillations of the reflectance and transmittance, which are of higher amplitude on the long wavelength side of the directional gap. The period (width) of the oscillation due to Fabry–Perot interference of a slab of finite thickness is related to the number of layers of the silica spheres. We note that the reflectance oscillations for the bare opal are buried in the noise. Comparing calculated results with the measured reflectance data corresponding to the infiltrated silica shown in figure 4, we found that the number of layers in that particular infiltrated sample is about 16. Changing the slab thickness will basically change the period of the oscillations, and the optical property will otherwise be qualitatively the same. We shall stick with a thickness of 16 layers in subsequent calculations.

The results in figure 4 show that as the infiltration proceeds, the main peak corresponding to the directional gap shifts to lower frequencies indicating an increase in the effective refractive

index in the voids. This increase has to come from the infiltration of Au. The TEM image (figure 2(d)) shows the infiltrated gold in the aperture to possess a random porous microstructure with particle size not larger than 40 nm. Given that the microstructure is much smaller than the wavelength, we describe the infiltrated gold complex structure inside the voids by using the Maxwell-Garnett model, which is the simplest of the effective medium theories [14]. The schematic diagram for the model is shown in figure 6. Within the framework of the Maxwell-Garnett model, the Au infiltrating material in the void is represented by an effective medium with the dielectric function ε_{eff} determined from $\frac{\varepsilon_{\text{eff}}-\varepsilon_{\text{b}}}{\varepsilon_{\text{eff}}+2\varepsilon_{\text{b}}} = f\frac{\varepsilon_{\text{Au}}-\varepsilon_{\text{b}}}{\varepsilon_{\text{Au}}+2\varepsilon_{\text{b}}}$, in which ε_{Au} is the dielectric function of Au, ε_{b} is the dielectric function of the supporting background. For simplicity, we take $\varepsilon_{\text{b}} = 1$, and ε_{Au} is taken from experimental data [13]. Once a particular Au filling ratio is specified, the effective dielectric function can be found and the spectra can be calculated with the multiple-scattering method. The Maxwell-Garnett formula is useful for systems in which the particles are very small compared with the wavelength and the filling ratio is small. We will show in the appendix that the Maxwell-Garnett formula did provide a very good ε_{eff} for 40 nm Au spheres up to a modest filling ratio of about 30%.

In figure 7, we show the reflectance and transmittance calculated for the configuration shown in figure 6, using an effective medium description of the infiltration material containing Au particles inside the void. The results show that as the filling ratio of gold increases, the directional gap shifts to longer wavelength, while the period of oscillation on the long wavelength side is only slightly modified. This is consistent with the experimental observation, which finds the partial gap shifting to longer wavelength as the plating time increases. It is difficult to determine the amount of gold that is infiltrated into the voids of the silica spheres by experiment alone, since the electroplating process is found to deposit Au in the top and the bottom plates. However, by comparing the calculation results and the experiment data, we can determine the filling ratio of gold within the context of the Maxwell-Garnett model. Our calculations show that the result obtained from the effective medium with 15% gold particles in vacuum fits the shift of the partial gap of the last experiment data well. This small filling ratio is consistent with the assumption of the Maxwell-Garnett model, which is valid in the limit of low concentrations and small particles.

A common feature of the long time reflectance spectra (see for example line 6 of figure 4(a)) is that there is an increase of reflectance compared with the short infiltration time reflectance. Another feature of the experimental data shown in figure 5 is that the dotted and dash–dotted curves (labelled as 2 and 3) are measured at different positions of the same sample, and yet we can see that the reflectance and transmittance are not the same. They have nearly the same wavelength of the reflectance peak that marks the position of the direction gap, and also the same period of the oscillation on the long wavelength side of the gap, but the amplitude of the oscillation is different. The reflection amplitude is nearly the same on the short wavelength side of the gap, but is different on the long wavelength side (see figure 5). The fact that curves 2 and 3 have nearly the same reflection peaks and oscillation periods implies that the sample thickness and the effective dielectric properties (gold concentration) in the voids are nearly the same in these two measured positions. Inspection under an optical microscope indicates that there is a thin layer of gold covering the surface of the slab. In order to see whether the thin capping can account for the observation, we model theoretically the effect of a thin top capping and bottom layer. Within the multiple-scattering formulation, we can add a pure gold plate at the top or at the bottom (see figure 6). Figure 8 shows the effect of a bottom layer of Au, of different thickness from 10 to 25 nm (the top side is clean); this is shown for a 16-layer Au-infiltrated slab. We see that a gold layer at the bottom increases the amplitude of the oscillation of the reflectance (figure 8), and the thicker the Au bottom layer, the stronger the oscillation. This is not surprising since the oscillations originate from a Fabry–Perot resonance effect that increases when the

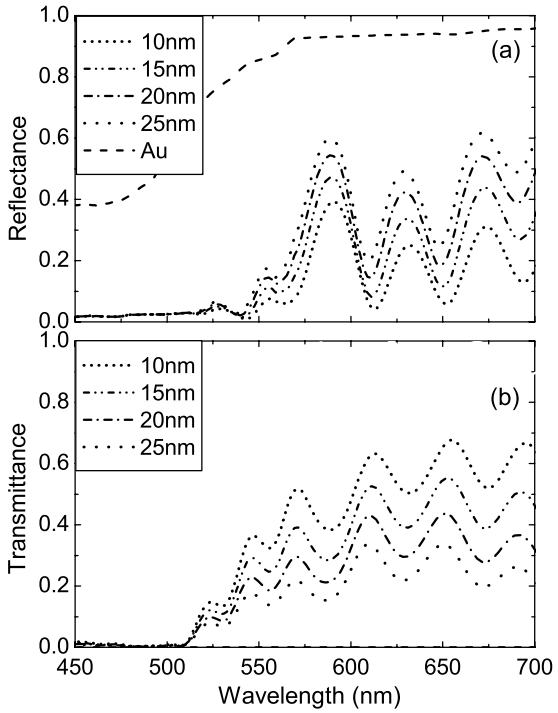

Figure 8. Calculated reflectance and transmittance of a 16-layer Au-infiltrated silica opal with an effective Au filling ratio of 15% and a thin layer of Au at the bottom of various thicknesses. The dashed line labelled Au is that for a pure Au slab of 0.5 μm. We note that the amplitude of the oscillation in the reflectance increases with the thickness of the bottom layer.

bottom interface becomes a better reflector as the Au layer thickness increases. Figure 9 shows the effect of adding a top capping layer of Au, while keeping the bottom clean. We see that the top Au layer increases the average value of the reflectance. The thicker the Au capping layer, the stronger the reflection. For comparison, we show the calculated reflectance of a 0.5 μm slab of gold. We see that the calculated reflectance agrees very well with the measured data shown in figure 5. In figure 9, we observe that as the overall reflectance increases with the thickness, the amplitude of the reflectance oscillation decreases but the decrease is very moderate. We also note that there is always a floor level for the reflectance (which is never zero) if there is a top capping layer of Au, while the minimum value of the reflectance can be zero if there is only a bottom layer of Au (see figure 8). Also, the amplitude of the reflection oscillation increases with the Au layer thickness if it is at the bottom, but decreases with the thickness when it is on the top. We also did calculations in which there are thin Au layers on both sides of the slab. While the results depend on the detailed configuration and combination of thickness parameters, the salient features of the results can be summarized as follows: a top Au layer basically governs the overall reflection, and in particular the reflection on the short wavelength side of the directional gap. The reflectance on the short wavelength side (where the oscillation is small) is very much indicative of the thickness of the top layer. On the other hand, the bottom Au layer contributes to the amplitude of the reflectance oscillation on the long wavelength side of the directional gap. It does not contribute much to the reflectance on the short wavelength side.

From figure 5(a), we note that the reflectance never reaches zero, and is of the order of 10% on the short wavelength side. The measured reflectance is thus consistent with the existence of

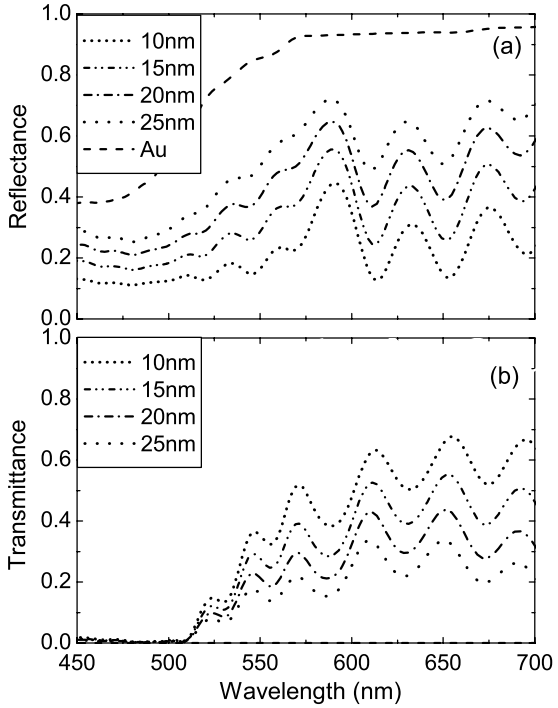

Figure 9. Calculated reflectance and transmittance of a 16-layer Au-infiltrated silica opal with an effective Au filling ratio of 15% and a top Au capping layer of various thicknesses. The dashed curve labelled Au is that for a pure Au slab of 0.5 μm. We note in the reflectance spectra that for the existence of a capping layer, the average reflectance increases as the capping layer increases in thickness, while the amplitude of the oscillation in the reflectance decreases with thickness.

a thin layer of Au above the opal slab, and, comparing with the calculated results, the thickness of the Au capping layer is of the order of 10 nm for the sample shown in figure 5. The fact that line 2 has a stronger oscillation amplitude than line 3 can be explained by the existence of a very thin coating of Au on the bottom, which is not uniform, so that the oscillation amplitude is position different. A thin layer of compact Au at the bottom is also consistent with the fact that the Fabry–Perot oscillations are much more conspicuous for the infiltrated samples than the clean silica opal. We also note from figures 8(b) and 9(b) that the transmittance is essentially the same for a top capping layer and a bottom layer of the same thickness, and thus the information is mainly contained in the reflectance spectra.

A closer look at figures 8 and 9 shows that the main reflectance peaks shift slightly to shorter wavelengths when there is a thin layer of Au on either side of the infiltrated opal slab. This is not surprising since the Au dielectric constant has a negative real part in the optical frequencies, and, in the long wavelength limit, this negative dielectric constant partly compensates the positive dielectric constant of the infiltrated silica. We see from figure 4, as the infiltration time goes from 10 to 300 s, that the main reflectance peak (corresponding to the directional gap) shows a gradual shift to longer wavelength, while the average reflectance (note in particular the shorter wavelength side of the main peak) does not increase. The reflectance measured at the longest time (600 s, line 6 in figure 4(a)), shows a conspicuous increase in reflectance, and the main reflectance peak actually shifts to a shorter wavelength compared with the reflectance measured at 300 s. The initial red shift can be accounted for by the gradual

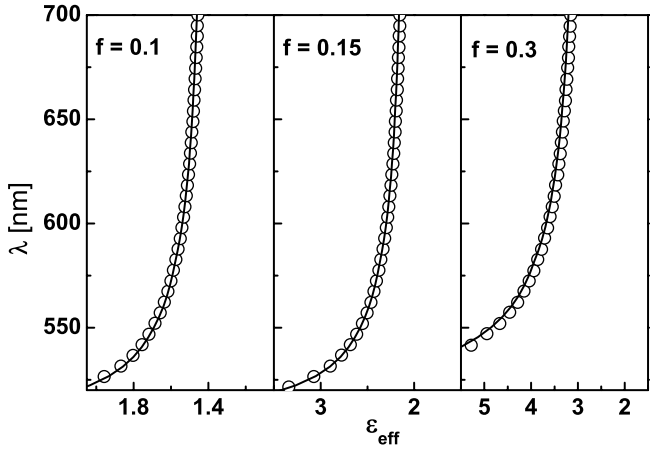

Figure 10. Effective dielectric constants for an FCC lattice of 40 nm (diameter) Au nanospheres in a host material of $\varepsilon_b = 1$ for three filling ratios of the spheres ($f = 0.1$, 0.15, and 0.3). The solid lines are calculated using the Maxwell-Garnett formula and the open circles are calculated numerically using the multiple-scattering formalism.

filling up of the voids with some Au particles, leading to a higher effective dielectric constant of the background. But after some time (about 300 s), probably when some connecting pathways are established between the top and bottom surfaces of the slab, the Au will be transported to the top, forming a thin Au layer there. This Au capping layer accounts for the blue shift of the reflectance peak and the overall increase of the reflectance. Apparently the Au deposition at the top is a rather efficient process once some percolation pathways are established, leaving a relatively small amount of Au deposition in the voids.

4. Summary

We applied an electroplating process to deposit Au in the voids of a silica opal formed using a force packing method. The results demonstrate that the effective dielectric properties of the voids were modified by the Au infiltration, leading to a change of optical characteristics that can be explained by numerical modelling using a multiple-scattering technique. The complex spectra of the composite system correspond reasonably well with the theoretical predictions, leading to an understanding of the measured optical properties in terms of the system microstructures.

Acknowledgments

We acknowledge the financial support of RGC Hong Kong grants HKUST6122/98P, HKUST6145/00P, HKUST6138/00P, and CA02/03SC01.

Appendix

We examine here whether the Maxwell-Garnett form of the effective medium theory [14] can describe the effective optical properties of a medium containing nano-Au particles with diameters of 40 nm. To this end, we consider a model system with 40 nm diameter Au nanospheres arranged in an FCC lattice and embedded in a host of $\varepsilon_b = 1$. The dispersion

(i.e. frequency versus wavevector) of this system can be calculated to a very high precision (essentially exactly) using the multiple-scattering method. The dispersion is then written as $n_{\text{eff}}\omega = ck$, where n_{eff} is the effective refractive index, ω is the frequency, and k is the Bloch wavevector. In our calculations, we fix ω and solve for the k. This gives the effective refractive index n_{eff} as a function of frequency (or wavelength) and hence we can find the effective dielectric constant as $\varepsilon_{\text{eff}} = n_{\text{eff}}^2$. The numerically calculated ε_{eff} for three filling ratios of Au nanospheres ($f = 0.1, 0.15, 0.3$) are shown in figure 10 and compared with the ε_{eff} obtained using the simple Maxwell-Garnett formula. For these comparisons, the imaginary part of the Au dielectric function is set to zero; otherwise, the dispersion is not well defined. We see that the Maxwell-Garnett formula does provide a very good ε_{eff} for 40 nm Au spheres up to a modest filling ratio of about 30%. The effective medium theory would be even better if the nanoparticles were smaller. Of course, we understand that Maxwell-Garnett theory is quantitatively correct only if the particles are distributed randomly. If the distribution is correlated, it requires correction. However, the detailed structural correlation of the Au nanoparticles is not known, and as we are aiming for a qualitative interpretation of the data, we will settle for the simplest model. For the same reason, we set the background ε_{b} of the Au nanoparticle as 1. Changing this background to another dielectric will only lead to minor quantitative changes, and the qualitative results remain the same.

References

[1] See, for example
Soukoulis C M (ed) 1996 *Photonic Band Gap Materials* (Dordrecht: Kluwer)
Yablonovitch E 1987 *Phys. Rev. Lett.* **58** 2059
John S 1987 *Phys. Rev. Lett.* **58** 2486
Joannopoulos J D, Meade R D and Winn J 1995 *Photonic Crystals* (Princeton, NJ: Princeton University Press)

[2] See, e.g.,
Cheng C C *et al* 1996 *Phys. Scr.* T **68** 17
Noda S and Sasaki A 1997 *Japan. J. Appl. Phys.* **36** 1907
Lin S Y *et al* 1998 *Nature* **394** 251

[3] For a review, see, e.g., van Blaaderen A 1998 *Science* **282** 887 and references therein

[4] Campbell M *et al* 2000 *Nature* **404** 53–6
Wang X *et al* 2003 *Appl. Phys. Lett.* **82** 2212–4
Wang X *et al* 2003 *Adv. Mater.* **15** 1526–8

[5] See, e.g., McCalmont J S *et al* 1996 *Appl. Phys. Lett.* **68** 2759
Sievenpiper D F, Sickmiller M E and Yablonovitch E 1996 *Phys. Rev. Lett.* **76** 2480

[6] Zhang W Y, Lei X Y, Wang Z L, Zheng D G, Tam W Y, Chan C T and Sheng P 2000 *Phys. Rev. Lett.* **84** 2853

[7] This electroplating technique has been recently used for deposition of metals or semiconductors onto sphere templates. See e.g.,
Xu L *et al* 2000 *Chem. Commun.* 997
Bartlett P N *et al* 2000 *Chem. Commun.* 1671
Luo Q *et al* 2001 *Adv. Mater.* **13** 286
Braun P V and Wiltzius P 2001 *Adv. Mater.* **13** 482

[8] Stöber W, Fink A and Bohn E 1968 *J. Colloid Interface Sci.* **26** 62

[9] Park S H and Xia Y 1999 *Langmuir* **15** 266

[10] Jiang Y *et al* 2003 *J. Phys.: Condens. Matter* **15** 5871

[11] Stefanou N, Yannopapas V and Modinos A 1998 *Comput. Phys. Commun.* **113** 49
Stefanou N, Yannopapas V and Modinos A 2000 *Comput. Phys. Commun.* **132** 189

[12] Yannopapas V, Modinos A and Stefanou N 1999 *Phys. Rev.* B **60** 5359

[13] The data for gold is obtained from Johnson P B and Christy R W 1972 *Phys. Rev.* B **6** 4370

[14] See, e.g., Choy T C 1999 *Effective Medium Theory: Principles and Applications* (Oxford: Oxford University Press)